ChemPhysMater 5 (2026) 485–492

Contents lists available at ScienceDirect

ChemPhysMater

journal homepage: https://www.keaipublishing.com/en/journals/chemphysmater/

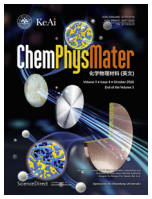

Research Article

Tight-binding and NEGF analysis of high-performance thermoelectric transport in MXene nanoribbons

Omid Soltani [a], Mohammad Reza Jafari [a,*], Aliasghar Shokri [b,*]

[a] Department of Condensed Matter Physics, Faculty of Physics, Alzahra University, Tehran 1993893973, Iran
[b] Department of Theoretical and Nano Physics, Faculty of Physics, Alzahra University, Tehran 1993893973, Iran

ARTICLE INFO

Keywords:
MXene device
Tight-binding approximation
Non-equilibrium green's function (NEGF)
Thermoelectric
Low-dimensional materials

ABSTRACT

The electronic thermoelectric properties of one-dimensional MXene nanoribbon devices were explored by adopting a tight-binding Hamiltonian coupled with the non-equilibrium Green's function (NEGF) formalism. The model device configuration involves finite $Ti_3C_2O_2$, $Sc_3C_2F_2$, and $Zr_3C_2O_2$ nanoribbon channels connected to graphene electrodes. Calculations of the temperature-dependent electronic thermoelectric coefficient were performed in order to obtain the figure of merit (ZT_e) for the electronic contribution, Seebeck coefficient, power factor, and normalized conductance (G/G_0). The results revealed that the best p-type performance of $Ti_3C_2O_2$ is attained at $\mu = 0.89$ eV, yielding very high ZT_e values of 4.9 at 300 K and up to 5.5 at 500 K. On the other hand, $Zr_3C_2O_2$ shows the strongest n-type response, with a ZT_e of approximately 4.7 at 300 K and with the highest conductance compared to all other studied systems. $Sc_3C_2F_2$ also presents a promising n-type performance with a maximum ZT_e of approximately 3.3 at 300 K. In all the studied structures, the power factors remained moderate due to the limited number of conducting channels available in finite one-dimensional nanoribbons. These results lead to an overall, consistent assessment of the electronic thermoelectric properties across different MXene nanoribbon compositions.

1. Introduction

The conversion of waste heat into electricity addresses energy efficiency challenges in modern technology. Thermoelectric materials enable direct energy conversion through the Seebeck effect, providing solid-state solutions for power generation and thermal management [1,2]. However, optimizing the interdependent electrical and thermal transport properties remains a fundamental challenge in developing high-performance thermoelectric materials [3].

Two-dimensional (2D) materials have emerged as promising candidates for thermoelectric applications due to their unique electronic and thermal transport properties. The quantum confinement effect in 2D/1D materials can enhance the power factor by modifying the density of states, while increased phonon boundary scattering reduces lattice thermal conductivity [4–9]. However, the thermoelectric performance varies significantly among different 2D/1D materials. For instance, graphene exhibits outstanding electrical conductivity but suffers from low Seebeck coefficient due to its linear dispersion relation near the Dirac point, resulting in poor thermoelectric efficiency [10]. In contrast, transition metal dichalcogenides like MoS_2 demonstrate more balanced electrical and thermal transport properties with promising power factors [9,11]. Similarly, phosphorene shows anisotropic thermoelectric properties that can be engineered through crystal orientation [12].

Recent studies have demonstrated various strategies to enhance the thermoelectric performance of graphene and its derivatives. Edge modification can introduce localized states that increase the Seebeck coefficient while reducing phonon transport [13]. Defect engineering—such as vacancy creation or substitutional doping—breaks lattice symmetry and scatters phonons, lowering the lattice thermal conductivity without severely degrading electrical conductivity [14]. Double-bend nanostructures create additional phonon scattering centers and have been shown to suppress thermal conductance in graphene ribbons [15]. Isotope-doping further reduces phonon mean free paths by mass disorder, leading to a noticeable drop in lattice thermal conductivity [16]. Finally, constructing graphene-based heterojunctions tailors band alignment and carrier filtering, thereby improving the power factor [17]. Incorporating these approaches provides a rich toolbox for tuning the interdependent electrical and thermal transport properties of two-dimensional materials and sets the stage for the investigation of MX-based nanoribbons in this work.

These fundamental characteristics make 2D semiconductors particularly suitable for investigating thermoelectric transport mechanisms and developing high-performance devices.

* Corresponding authors.
E-mail addresses: mo.jafari@alzahra.ac.ir (M.R. Jafari), aashokri@alzahra.ac.ir (A. Shokri).

https://doi.org/10.1016/j.chphma.2026.04.001
Received 1 January 2026; Received in revised form 23 March 2026; Accepted 19 April 2026
Available online 30 April 2026
2772-5715/© 2026 The Authors. Publishing Services by Elsevier B.V. on behalf of KeAi Communications Co. Ltd. This is an open access article under the CC BY license (http://creativecommons.org/licenses/by/4.0/)

Among the family of two-dimensional materials, MXenes represent a rapidly expanding class of transition metal carbides, nitrides, and carbonitrides with the general formula $M_{n+1}X_nT_x$ that has attracted considerable attention for various energy applications [18]. Their unique combination of high electrical conductivity, tunable surface chemistry, and diverse elemental composition positions them as compelling candidates for thermoelectric investigations. Recent reviews have analyzed the progress and challenges in developing MXene-based thermoelectric materials, highlighting their unique layered structure and exceptional physical properties [19,20]. Initial studies have demonstrated their potential in this domain. For example, computational screening of MXenes has identified several compositions with promising thermoelectric properties that can be optimized through strategic selection of transition metals and surface functional groups [21–25]. Studies on ordered double transition metal MXenes, such as $Cr_2TiC_2T_2$, have predicted high Seebeck coefficients (S) and the figure of merit (ZT) values up to 3.0 [26]. Also, previous theoretical studies have investigated bulk Ti_3C_2 MXene properties using DFT calculations [27]. Experimental characterizations of $Ti_3C_2T_x$ MXenes have revealed decent Seebeck coefficients while maintaining metallic conductivity, suggesting their viability for thermoelectric applications [28,29]. Beyond the well-studied Ti-based MXenes, recent computational investigations have also explored the thermoelectric potential of Sc-containing MXenes. For instance, DFT studies on Sc_2CX_2 structures have predicted promising power factors, further supporting the investigation of scandium-based compositions in the MXene family [30,31]. More recent work on other MXene compositions, such as Mo_2CT_x and V_2CT_x, has further expanded the prospects of this materials family for thermoelectric energy conversion [32]. The extensive chemical diversity and controllable surface termination of MXenes offer multiple avenues for enhancing their thermoelectric performance through band engineering and phonon scattering optimization.

This computational study investigates the thermoelectric properties of three MXenes ($Zr_3C_2O_2$, $Sc_3C_2F_2$, $Ti_3C_2O_2$) using a multiscale approach. The tight-binding parameters, fitted from DFT calculations, are employed in combination with the non-equilibrium Green's function (NEGF) formalism to simulate quantum transport in nanodevices [33–37]. This methodology allows us to systematically examine how transition metal selection and surface termination affect electron transport properties. By analyzing the relationship between electronic structure and thermoelectric performance across these three compositions, we identify key design principles for achieving high ZT values. The results demonstrate that rational materials selection based on electronic properties can lead to exceptional thermoelectric performance, with ZT exceedingly nearly 5 in optimized structures.

The paper is organized as follows: In Section 1, we provide an introduction to MXenes, highlighting their unique properties and significance for thermoelectric and nanoelectronic applications. In Section 2, we employ a tight-binding model based on the Slater–Koster formalism to investigate the electronic structure and quantum transport properties of MXene nanodevices. The model parameters, including on-site energies and hopping integrals for $Ti_3C_2O_2$, $Sc_3C_2F_2$, and $Zr_3C_2O_2$, are carefully fitted to reproduce the corresponding first-principles DFT band structures, as detailed in this section. Section 3 presents the numerical results along with a comprehensive discussion of the calculated electronic transport and thermoelectric properties. Finally, Section 4 summarizes the main findings and concludes the paper.

2. Computational details

In this work, we employ a tight-binding model based on the Slater-Koster formalism to investigate the electronic and quantum transport properties of MXene nanodevices. The model parameters including hopping integrals and on-site energies for $Ti_3C_2O_2$, $Sc_3C_2F_2$, and $Zr_3C_2O_2$ were carefully fitted to reproduce first-principles DFT band structures, as detailed in Refs. [33–37]. Table 1 lists the tight-binding parameters employed in the 23-parameter model. This parameterization ensures that the electronic structure features, such as band gaps, are accurately captured. The lattice constants and interaction range up to the second nearest neighbors were also adopted from these references, maintaining consistency with ab initio predictions. The resulting tight-binding model thus provides a reliable and computationally efficient platform for quantum transport simulations, while retaining atomic-level accuracy. This approach significantly reduces computational cost and memory requirements compared to full first-principles quantum transport calculations, while maintaining essential physical insights, making investigation of multiple device configurations feasible.

Table 1
The Slater-Koster parameters in units of eV for $Ti_3C_2O_2$, $Sc_3C_2F_2$ and $Zr_3C_2O_2$ structures [33–37].

SK Parameter	$Ti_3C_2O_2$	$Sc_3C_2F_2$	$Zr_3C_2O_2$
E_Z	−1.100	−0.963	−0.642
$E_x = E_y$	−1.534	−1.062	−0.185
$E_{x^2-y^2} = E_{xy}$ (center M atom)	2.817	5.344	4.443
E_{z^2}	2.091	5.479	4.120
$E_{yz} = E_{zx}$ (center M atom)	4.392	6.513	5.832
$E_{x^2-y^2} = E_{xy}$	2.319	4.344	4.336
E_{z^2}	2.195	3.979	4.020
$E_{yz} = E_{zx}$	4.081	5.213	5.071
ppσ	0.282	0.390	0.472
ppπ	0.178	−0.047	0.394
ddσ (1NN)	−0.719	1.279	1.037
ddπ (1NN)	0.553	−0.239	0.131
ddδ (1NN)	−0.226	−0.164	−0.711
ddσ (2NN)	−0.439	0.472	0.456
ddπ (2NN)	−0.111	0.419	−0.247
ddδ (2NN)	0.050	−0.027	0.361
ddσ (center M atom)	−0.563	−0.389	0.898
ddπ (center M atom)	−0.129	0.073	0.233
ddδ (center M atom)	0.050	0.102	−0.238
pdσ (1NN)	0.430	−0.117	0.144
pdπ (1NN)	0.268	−0.111	0.484
pdσ (2NN)	0.591	−0.131	−0.934
pdπ (2NN)	0.716	−0.356	0.932

The central scattering region of the device is constructed from the MXene nanoribbon supercell containing 25 atoms, comprising 10 carbon atoms and 15 transition metal atoms. The electronic structure is described using a minimal orbital basis set: five d-orbitals for each metal atom and three p-orbitals for each carbon atom, resulting in a 105 × 105 Hamiltonian matrix that captures the essential electronic properties while maintaining computational efficiency.

The device is interfaced with semi-infinite zigzag graphene nanoribbon electrodes, where each electrode unit cell contains 12 atoms. The electrode Hamiltonian employs the same orbital basis representation, yielding compact 36 × 36 intra-cell and inter-cell Hamiltonian matrices that ensure efficient quantum transport calculations while maintaining accuracy in the electronic structure description. The zigzag graphene nanoribbons (ZGNRs) used as electrodes provide metallic charge injection and exhibit good experimental compatibility with MXene layers, as demonstrated in a variety of graphene–MXene heterostructures [38–41]. The width of the zigzag graphene nanoribbon electrodes controls the number of metallic sub-bands crossing the Fermi level. Increasing the ribbon index N adds sub-bands and raises the electronic conductance roughly linearly, whereas the Seebeck coefficient changes only marginally. Test calculations for $N = 8$, 12 and 16 show that the maximum electronic ZT varies by ≤ 0.05 and the optimal chemical potential shifts by ≤ 0.02 eV, indicating that the qualitative trends reported in the manuscript are robust against reasonable variations in electrode width. The chosen width $N = 12$ was selected to match the MXene channel width and to ensure metallic contact without affecting the main conclusions [42–44]. This carefully designed computational enables investigation of quantum transport phenomena while optimizing the balance between physical accuracy and computational requirements. The complete device architecture, illustrating the inte-

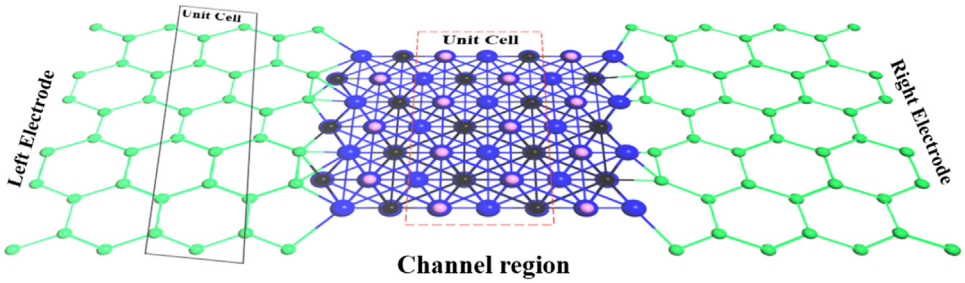

Fig. 1. Schematic top view of the proposed MXene-based thermoelectric device. The central scattering region consists of a MXene nanoribbon ($Zr_3C_2O_2$, $Sc_3C_2F_2$, or $Ti_3C_2O_2$), seamlessly connected to semi-infinite zigzag graphene nanoribbon electrodes on both ends. The unit cells of the graphene electrodes (black rectangle) and MXene channel (red dashed rectangle) are indicated, highlighting the atomic-scale integration between the different 2D materials in this hybrid structure.

gration between MXene channel and graphene electrodes, is presented in Fig. 1.

The electron transport properties were calculated using the NEGF formalism within the tight-binding framework. The retarded Green's function of the central device region is given by [45,46]

$$\mathbf{G}^{(r)}(E) = [E\mathbf{I} - \mathbf{H} - \mathbf{\Sigma}_L(E) - \mathbf{\Sigma}_R(E)]^{-1}, \quad (1)$$

where $\mathbf{H}$ is the Hamiltonian matrix of the central region, $\mathbf{I}$ is the identity matrix, and $\mathbf{\Sigma}_{L/R}$ are the self-energies of the left/right electrodes that incorporate the effects of the semi-infinite leads. The energy-dependent transmission coefficient, $T(E)$, was computed using [45]

$$T(E) = Tr\left[\mathbf{\Gamma}_L(E)\mathbf{G}^{(r)}(E)\mathbf{\Gamma}_R(E)\mathbf{G}^{(a)}(E)\right], \quad (2)$$

where $\mathbf{\Gamma}_{L/R}(E) = i[\mathbf{\Sigma}_{L/R}(E) - \mathbf{\Sigma}_{L/R}{}^{\dagger}(E)]$ is the coupling matrices, and $\mathbf{G}^{(a)}(E) = [\mathbf{G}^{(r)}(E)]^{\dagger}$ is the advanced Green's function.

The thermoelectric coefficients are evaluated using the moments of the transmission function via [47]

$$L_n = \frac{h}{2}\int_{-\infty}^{\infty} T(E)(E-\mu)^n\left(\frac{-\partial f}{\partial E}\right)\mathrm{d}E. \quad (3)$$

The electrical conductance, G, Seebeck coefficient, S, and electronic thermal conductance, κ_e were then calculated as [47,48]

$$G = e^2 L_0, \quad (4)$$

$$S = -\frac{1}{eT}\times\frac{L_1}{L_0}, \quad (5)$$

$$\kappa_e = \frac{1}{T}\left(L_2 - \frac{L_1^2}{L_0}\right). \quad (6)$$

The power factor, PF, and thermoelectric figure of merit, ZT, were determined using [45–49]

$$PF = S^2 G, \quad (7)$$

$$ZT = \frac{S^2 GT}{\kappa_e + \kappa_{ph}}. \quad (8)$$

In the present quasi-one-dimensional nanoribbon system, the lattice thermal conductivity (κ_{ph}) is expected to be drastically suppressed compared to its monolayer counterpart. This reduction stems from strong phonon-boundary scattering and the limited available phonon modes in confined geometries, a well-established trend in low-dimensional nanostructures [49–53]. For instance, while first-principles studies report the total thermal conductivity of MXene monolayers to be in the range of 54–105 W/mK with electrons contributing 37%–61% at 300 K [53], such values are not representative of nanoribbons.

Since our primary focus is on evaluating the electronic contribution to the thermoelectric performance, we treat κ_{ph} as a constant parameter in our calculations. To provide a conservative and physically reasonable estimate, we adopt κ_{ph} = 2.0 W/mK as our benchmark value, reflecting over an order of magnitude reduction from the monolayer limit. in low-dimensional MXene nanoribbons the lattice thermal conductivity is dominated by strong boundary scattering, leading to a weak temperature dependence; κ_{ph} typically varies by <20% between 100 and 500 K, justifying the use of a constant benchmark value of 2.0 W m^{-1} K^{-1} (taken at ≈300 K) [49–53]. This approach allows us to obtain an upper-bound estimate for the electronic figure of merit (ZT) while capturing the essential physics of nanoscale thermal transport.

All thermoelectric transport calculations were performed at temperatures of 100, 300, and 500 K. The chemical potential was varied across the Fermi level to map the electronic density of states' influence and identify optimal operating conditions for maximizing ZT.

3. Results and discussion

The thermoelectric response of a material is highly sensitive to the chemical potential (μ), which determines the occupancy of electronic states and thereby influences the Seebeck coefficient (S), electrical conductivity (σ), and the resulting dimensionless figure of merit (ZT) and power factor (PF). To identify the optimal operating condition, μ was scanned over the range [−1,1] eV at 300 K for $Ti_3C_2O_2$, $Sc_3C_2F_2$, and $Zr_3C_2O_2$ MXenes.

The variation of ZT with chemical potential shown in Fig. 2 can be attributed to the interplay between the Seebeck coefficient and the electrical conductivity. As the chemical potential shifts, the carrier concen-

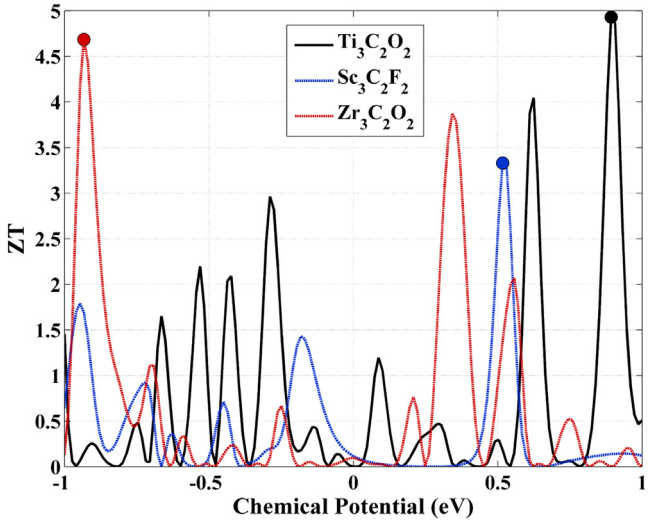

Fig. 2. Dependence of the thermoelectric figure of merit (ZT) on the chemical potential (μ) at 300 K for $Ti_3C_2O_2$, $Sc_3C_2F_2$, and $Zr_3C_2O_2$ MXenes. The optimal chemical potential (μ_{opt}) corresponding to the maximum ZT for each material is indicated by a filled marker.

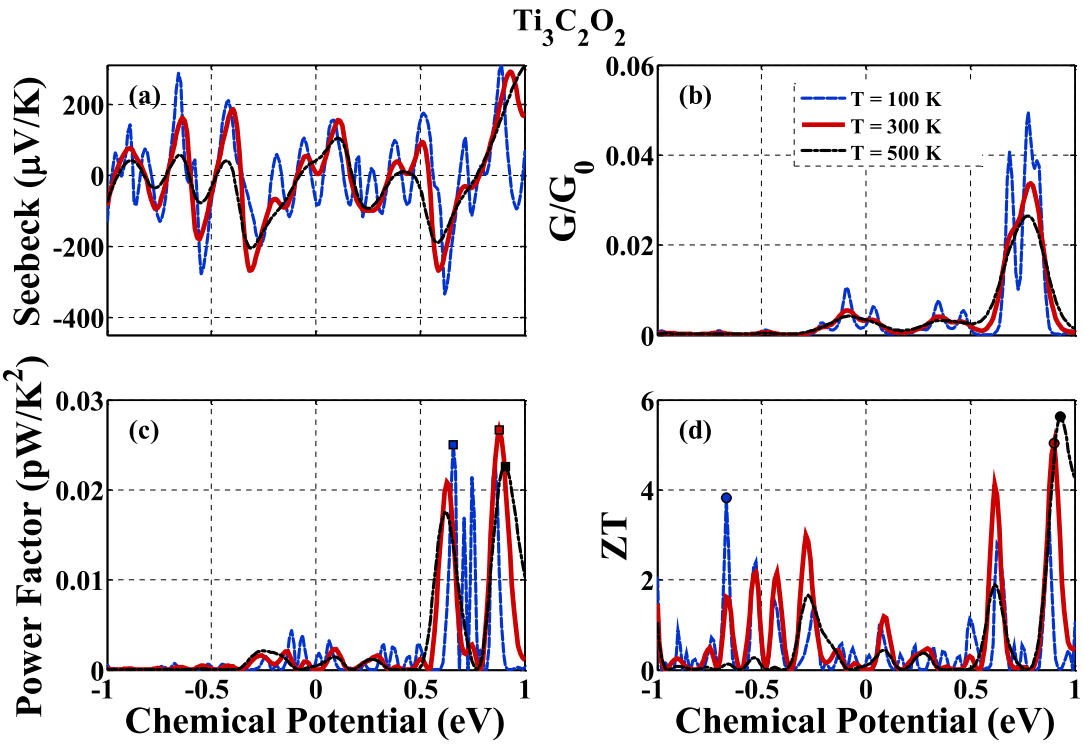

Fig. 3. Thermoelectric properties of $Ti_3C_2O_2$ MXene versus chemical potential: (a) Seebeck coefficient, (b) G/G_0, (c) power factor and (d) ZT at 100, 300, and 500 K.

tration changes, modifying the balance between these two transport parameters. At low carrier densities, the Seebeck coefficient is relatively high, but electrical conductivity is low, limiting ZT. Conversely, at high carrier densities, conductivity increases while the Seebeck coefficient decreases. The maximum ZT occurs at an intermediate chemical potential where the product of electrical conductivity and the square of the Seebeck coefficient is optimized. This general behavior explains the distinct μ_{opt} observed for each MXene materials.

Fig. 2 presents the computed thermoelectric performance of the three selected MXene materials as a function of chemical potential at 300 K. The variation of the dimensionless ZT with chemical potential illustrates distinct optimal values for each material. $Ti_3C_2O_2$ exhibits a maximum ZT at a positive chemical potential of 0.893 eV, indicating p-type conduction. $Sc_3C_2F_2$ also shows p-type behavior with its optimal chemical potential at 0.517 eV. Conversely, $Zr_3C_2O_2$ achieves its maximum ZT at a negative chemical potential of −0.933 eV, consistent with n-type conduction.

The observed differences in optimal chemical potentials reflect the electronic band structures and carrier concentrations of the materials. Positive chemical potentials correspond to a Fermi level closer to the conduction band, favoring electron transport, while negative chemical potentials correspond to a Fermi level closer to the valence band, favoring hole transport. The relative positions of the bands and the associated density of states govern the Seebeck coefficient and the resulting ZT values, as depicted in Fig. 2. Overall, the analysis highlights that the thermoelectric efficiency of MXenes can be tuned via chemical potential, which directly correlates with the type and concentration of charge carriers. These findings provide a foundation for further material optimization in thermoelectric applications.

Fig. 3 presents a comprehensive analysis of the thermoelectric properties of $Ti_3C_2O_2$ MXene as functions of chemical potential across temperatures of 100, 300, and 500 K. The panel (a) shows the Seebeck coefficient, revealing the characteristic dual behavior of $Ti_3C_2O_2$ with both positive and negative values depending on the chemical potential. The optimal p-type Seebeck coefficient reaches approximately 300 μV/K at room temperature. The panel (b) displays the normalized quantum conductance (G/G_0) as a function of chemical potential. The optimal conductance for all three temperatures occurs at approximately 0.8 eV, with the maximum values decreasing with increasing temperature: 0.05 G_0 at 100 K, 0.033 G_0 at 300 K, and 0.026 G_0 at 500 K. This temperature-dependent reduction in conductance suggests enhanced electron scattering mechanisms at higher temperatures, while the consistent optimal chemical potential indicates stable electronic transport characteristics across the studied temperature range. The observed temperature-dependent reduction in quantum conductance arises from thermal broadening of the Fermi-Dirac distribution, which diminish ballistic transport efficiency at elevated temperatures.

The panel (c) presents the power factor as a function of chemical potential. The optimal power factor occurs in the chemical potential range of 0.6–0.8 eV across all temperatures, with the highest value of 0.027 pW/K^2 achieved at 300 K. This optimal performance window represents a balance between the high Seebeck coefficient and substantial electrical conductance in this region. The superior performance at room temperature suggests that $Ti_3C_2O_2$ is particularly well-suited for practical applications operating near ambient conditions. Panel (d) shows the dimensionless figure of merit as a function of chemical potential. Remarkably, the highest ZT value of 5.5 is achieved at 500 K, followed by 4.9 at 300 K and 3.8 at 100 K, demonstrating enhanced thermoelectric performance at elevated temperatures. The optimal chemical potentials are −0.67 eV for 100 K, 0.89 eV for 300 K, and 0.91 eV for 500 K, indicating a gradual shift toward more positive potentials with increasing temperature. This temperature-dependent optimization suggests that carrier concentration tuning through chemical potential adjustment can maximize ZT across different operating temperatures.

Fig. 4 presents a comprehensive analysis of the thermoelectric properties of $Sc_3C_2F_2$ MXene. Panel (a) shows the Seebeck coefficient, revealing dual behavior with p-type characteristics ($S \approx +200$ μV/K) at $\mu = -0.172$ eV and superior n-type performance ($S \approx -250$ μV/K) at $\mu = 0.517$ eV. The optimal n-type response demonstrates its potential as an efficient n-type thermoelectric material. Panel (b) displays the G/G_0, where the optimal conductance for all three temperatures occurs at ap-

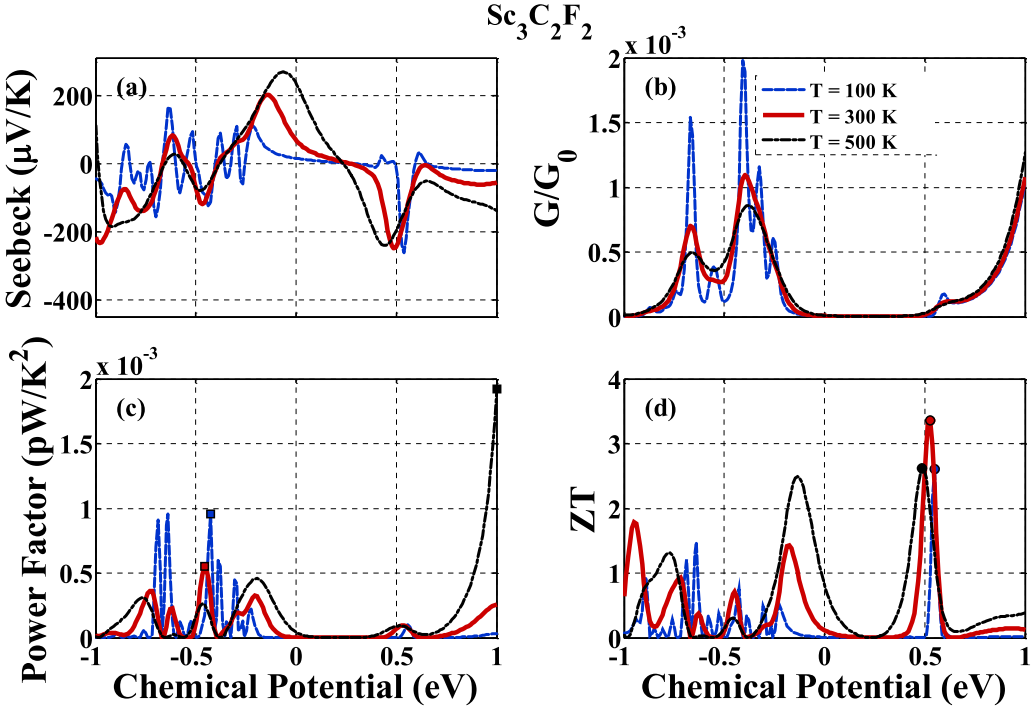

Fig. 4. Thermoelectric properties of $Sc_3C_2F_2$ MXene versus chemical potential: (a) Seebeck coefficient, (b) G/G_0, (c) power factor and (d) ZT at 100, 300, and 500 K.

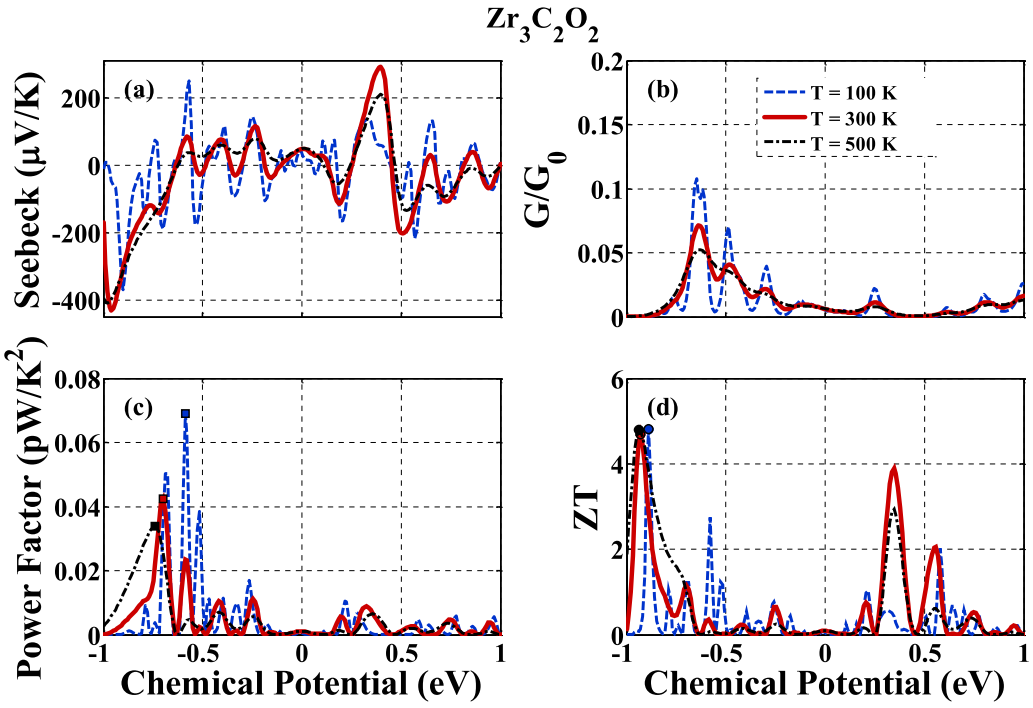

Fig. 5. Thermoelectric properties of $Zr_3C_2O_2$ MXene versus chemical potential: (a) Seebeck coefficient, (b) G/G_0, (c) power factor and (d) ZT at 100, 300, and 500 K.

proximately $\mu = -0.38$ eV, with values on the order of 10^{-3} G_0, significantly lower than $Ti_3C_2O_2$, indicating more restricted electronic transport in this MXene. Panel (c) illustrates the power factor, demonstrating optimal performance at room temperature around $\mu = -0.4$ eV, resulting from favorable interplay between the Seebeck coefficient and electrical conductance. Panel (d) presents the dimensionless figure of merit, achieving values between 0.4–0.6 eV, with the highest value of 3.3 at room temperature, confirming $Sc_3C_2F_2$ as a promising n-type thermoelectric material.

Fig. 5 presents a comprehensive analysis of the thermoelectric properties of $Zr_3C_2O_2$ MXene. Panel (a) shows the Seebeck coefficient, demonstrating exceptional n-type thermoelectric characteristics with a remarkably high Seebeck coefficient exceeding −400 μV/K at the optimal chemical potential of −0.933 eV. This adjective performance, combined with its negative chemical potential alignment, positions $Zr_3C_2O_2$ as a premier n-type candidate for room-temperature thermoelectric applications. Panel (b) displays the normalized quantum conductance, where the maximum conductance of 0.07 G_0 occurs at $\mu = -0.62$ eV

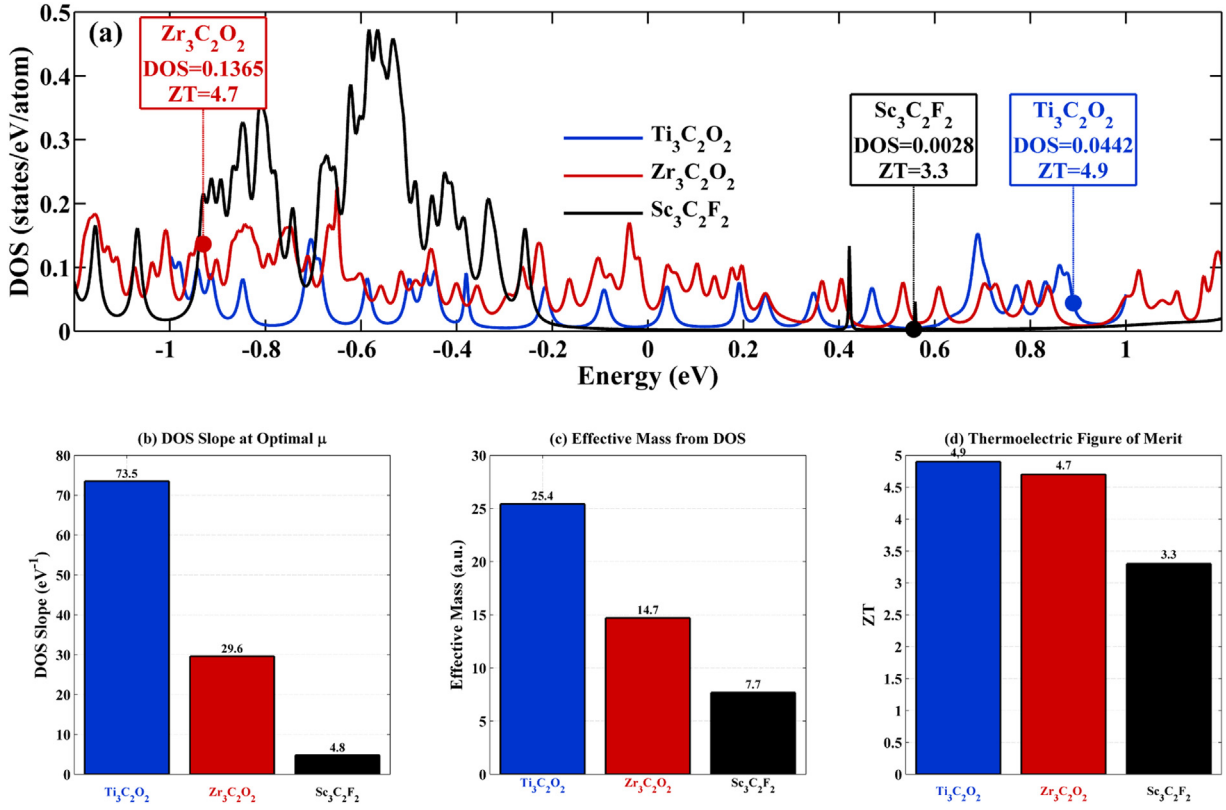

Fig. 6. Physical analysis of the thermoelectric behavior of $Ti_3C_2O_2$, $Zr_3C_2O_2$, and $Sc_3C_2F_2$ nanoribbons. (a) DOS at the chemical potentials corresponding to maximum *ZT*. (b) DOS slope at optimal μ, indicating differences in Seebeck response. (c) Effective mass extracted from DOS curvature. (d) Maximum *ZT* values showing the performance ranking among the three structures.

at room temperature, representing the highest conductance among the three studied MXenes. Panel (c) illustrates the power factor, showing optimal performance in the chemical potential range of −0.6 to −0.8 eV across different temperatures, with the highest value slightly exceeding 0.04 pW/K^2 at room temperature. Finally, panel (d) presents the *ZT*, achieving a maximum value of 4.7 at room temperature at $\mu = -0.93$ eV, confirming $Zr_3C_2O_2$ as an outstanding n-type thermoelectric material with exceptional overall performance.

Fig. 6 presents a comparative analysis of the electronic and thermoelectric characteristics of $Ti_3C_2O_2$, $Zr_3C_2O_2$, and $Sc_3C_2F_2$ nanoribbons, focusing on the role of their density of states (DOS) in determining transport performance. The DOS profiles at the chemical potentials corresponding to maximum *ZT* show distinct differences among the three systems has been shown in the panel (a). $Ti_3C_2O_2$ exhibits a sharp and high-slope DOS feature near the optimal μ, while $Zr_3C_2O_2$ presents moderately broadened peaks and $Sc_3C_2F_2$ shows a comparatively flat DOS. These contrasts indicate that the local DOS structure near μ strongly influences the achievable Seebeck coefficient and thus *ZT*.

According to the panel (b), the extracted DOS slopes at the optimal chemical potential highlight this trend more clearly: $Ti_3C_2O_2$ shows the largest slope, $Zr_3C_2O_2$ an intermediate value, and $Sc_3C_2F_2$ the smallest. Since the Seebeck coefficient in such systems is directly linked to $\partial(\mathrm{DOS})/\partial E$, these results provide a quantitative explanation for the observed ordering of thermoelectric performance. It can be seen from panel (c) that the effective masses obtained from the DOS curvature further confirm this correlation. $Ti_3C_2O_2$ has the highest effective mass, $Zr_3C_2O_2$ follows, and $Sc_3C_2F_2$ has the lowest value. Higher effective mass generally corresponds to stronger localization and enhanced DOS near band edges, which is consistent with the enhanced thermoelectric response.

From panel (d), we can find that the resulting *ZT* values reflect the combined influence of DOS sharpness and effective mass: $Ti_3C_2O_2$ exhibits the highest *ZT*, $Zr_3C_2O_2$ shows moderately high performance, and $Sc_3C_2F_2$ yields the lowest.

The electrical conductance (*G*) directly influences the thermoelectric efficiency because it determines the power factor, which is the product of *G* and the square of the Seebeck coefficient. In our calculations a larger *G* increases the power factor and therefore raises the figure of merit (*ZT*), provided that the Seebeck coefficient does not drop dramatically. Consequently, the optimal *ZT* is achieved when the increase in conductance is balanced by a still-appreciable Seebeck coefficient. For the MXene nanoribbons studied, the peak thermoelectric performance coincides with the range where the conductance rises steeply while the Seebeck coefficient remains sizable, confirming the expected positive correlation between *G* and thermoelectric performance.

This alignment across all panels demonstrates that the thermoelectric efficiency of these MXene nanoribbons is predominantly governed by the energy dependence of the DOS around the operating chemical potential.

4. Conclusions

Our results demonstrate that MXene nanoribbons exhibit significant thermoelectric potential within the 100–500 K temperature range. $Ti_3C_2O_2$ shows its highest p-type performance at $\mu = 0.89$ eV, reaching Seebeck coefficients near 300 μV/K and *ZT* values of 3.8 at 100 K, 4.9 at 300 K, and 5.5 at 500 K. $Zr_3C_2O_2$ performs most effectively under n-type conditions, achieving a *ZT* of 4.7 at 300 K, with Seebeck coefficients below −400 μV/K at $\mu = -0.93$ eV and the highest conductance (0.07 G_0) among the three systems. $Sc_3C_2F_2$ also delivers competitive n-type performance, reaching a *ZT* of 3.3 at 300 K, while maintaining tunability across different chemical potentials. The distinct temperature-dependent behaviors $Ti_3C_2O_2$ with increasing *ZT* at higher temperatures, $Zr_3C_2O_2$ with stable and balanced performance over a broad win-

dow, and $Sc_3C_2F_2$ with consistently strong n-type response highlight the flexibility of MXene nanoribbons for thermoelectric optimization. These characteristics indicate that reduced-dimensional MXenes can serve as versatile platforms for designing efficient thermoelectric and thermal-energy-harvesting devices.

Code and data availability

MATLAB code for computational study of MXene transport properties under bias and temperature variations is available on GitHub [54].

Declaration of Competing Interest

The authors declare that they have no known competing financial interests or personal relationships that could have appeared to influence the work reported in this paper.

CRediT authorship contribution statement

Omid Soltani: Writing – original draft, Visualization, Validation, Project administration, Methodology, Investigation, Data curation, Conceptualization. **Mohammad Reza Jafari:** Writing – review & editing, Visualization, Project administration, Investigation, Conceptualization. **Aliasghar Shokri:** Writing – review & editing, Visualization, Validation, Project administration, Methodology, Investigation, Data curation, Conceptualization.

Acknowledgements

This work is based upon research funded by Iran National Science Foundation (INSF) under project No. 4041916.

References

[1] J. He, T.M. Tritt, Advances in thermoelectric materials research: Looking back and moving forward, Science 357 (2017) eaak9997, doi:10.1126/science.aak9997.
[2] A. Shakouri, Recent developments in semiconductor thermoelectric physics and materials, Annu. Rev. Mater. Res. 41 (2011) 399–431, doi:10.1146/annurev–matsci-062910-100445.
[3] G.J. Snyder, E.S. Toberer, Complex thermoelectric materials, Nat. Mater. 7 (2008) 105–114, doi:10.1038/nmat2090.
[4] G. Zhang, Y.W. Zhang, Thermoelectric properties of two-dimensional transition metal dichalcogenides, J. Mater. Chem. C 5 (2017) 7684–7698, doi:10.1039/C7TC01088E.
[5] G.Z. Qin, X.L. Zhang, S.Y. Yue, Z.Z. Qin, H.M. Wang, Y. Han, M. Hu, Resonant bonding driven giant phonon anharmonicity and low thermal conductivity of phosphorene, Phys. Rev. B 94 (2016) 165445, doi:10.1103/PhysRevB.94.165445.
[6] H. Sadeghi, S. Sangtarash, C.J. Lambert, Enhanced thermoelectric efficiency of porous silicene nanoribbons, Sci. Rep. 5 (2015) 9514, doi:10.1038/srep09514.
[7] A. Shokri, N. Salami, Gas sensor based on MoS_2 monolayer, Sens. Actuators B 235 (2016) 678–690, doi:10.1016/j.snb.2016.05.129.
[8] F.M. Mousavi, R. Farghadan, Thermoelectric properties in twisted bilayer zigzag graphene nanoribbons, J. Phys. Chem. Solids 208 (2026) 113032, doi:10.1016/j.jpcs.2025.113032.
[9] A. Shokri, N. Salami, Thermoelectric properties in monolayer MoS_2 nanoribbons with Rashba spin-orbit interaction, J. Mater. Sci. 54 (2019) 467–482, doi:10.1007/s10853-018-2837-8.
[10] Y. Xu, Z. Li, W. Duan, Thermal and thermoelectric properties of graphene, Small 10 (2014) 2182–2199, doi:10.1002/smll.201303701.
[11] K. Hippalgaonkar, Y. Wang, Y. Ye, D.Y. Qiu, H.Y. Zhu, Y. Wang, J. Moore, S.G. Louie, X. Zhang, High thermoelectric power factor in two-dimensional crystals of MoS_2, Phys. Rev. B 95 (2017) 115407, doi:10.1103/PhysRevB.95.115407.
[12] R.X. Fei, A. Faghaninia, R. Soklaski, J.A. Yan, C. Lo, L. Yang, Enhanced thermoelectric efficiency via orthogonal electrical and thermal conductances in phosphorene, Nano Lett. 14 (2014) 6393–6399, doi:10.1021/nl502865s.
[13] Z.X. Xie, X.K. Chen, X. Yu, Y.X. Deng, Y. Zhang, W.X. Zhou, P.Z. Jia, Atomistic simulation of thermoelectric properties in cove-edged graphene nanoribbons, J. Appl. Phys. 135 (2024) 024302, doi:10.1063/5.0184595.
[14] Z.X. Xie, Y. Zhang, L.F. Zhang, D.Y. Fan, Effect of topological line defects on electron-derived thermal transport in zigzag graphene nanoribbons, Carbon 114 (2017) 383–392, doi:10.1016/j.carbon.2016.11.064.
[15] K.M. Li, Z.X. Xie, K.L. Su, W.H. Luo, Y. Zhang, Ballistic thermoelectric properties in double-bend graphene nanoribbons, Phys. Lett. A 378 (2014) 1536–1539, doi:10.1016/j.physleta.2014.03.023.
[16] Z.X. Xie, X.K. Chen, X. Yu, Y. Zhang, H.B. Wang, L.F. Zhang, Reduction of phonon thermal conduction in isotopic graphene nanoribbon superlattices, Sci. China Phys. Mech. Astron. 60 (2017) 107821, doi:10.1007/s11433-017-9080-0.
[17] P.Z. Jia, Y.J. Zeng, D. Wu, H. Pan, X.H. Cao, W.X. Zhou, Z.X. Xie, J.X. Zhang, K.Q. Chen, Excellent thermoelectric performance induced by interface effect in $MoS_2/MoSe_2$ van der Waals heterostructure, J. Phys. Condens. Matter. 32 (2020) 055302, doi:10.1088/1361-648X/ab4cab.
[18] B. Anasori, M.R. Lukatskaya, Y. Gogotsi, 2D metal carbides and nitrides (MXenes) for energy storage, Nat. Rev. Mater. 2 (2017) 16098, doi:10.1038/natrevmats.2016.98.
[19] M. Zhu, C. Lu, L. Liu, Progress and challenges of emerging MXene based materials for thermoelectric applications, iScience 26 (2023) 106718, doi:10.1016/j.isci.2023.106718.
[20] S. Bandaru, A.M. Jastrzębska, M. Birowska, Recent progress in thermoelectric MXene-based structures versus other 2D materials, Appl. Mater. Today 34 (2023) 101902, doi:10.1016/j.apmt.2023.101902.
[21] M. Khazaei, M. Arai, T. Sasaki, C.Y. Chung, N.S. Venkataramanan, M. Estili, Y. Sakka, Y. Kawazoe, Novel electronic and magnetic properties of two-dimensional transition metal carbides and nitrides, Adv. Funct. Mater. 23 (2013) 2185–2192, doi:10.1002/adfm.201202502.
[22] Z. Guo, J. Zhou, Z. Sun, New two-dimensional transition metal borides for Li ion batteries and electrocatalysis, J. Mater. Chem. A 5 (2017) 23530–23535, doi:10.1039/C7TA08665B.
[23] H. Kim, B. Anasori, Y. Gogotsi, H.N. Alshareef, Thermoelectric properties of two-dimensional molybdenum-based MXenes, Chem. Mater. 29 (2017) 6472–6479, doi:10.1021/acs.chemmater.7b02056.
[24] M. Khazaei, M. Arai, T. Sasaki, M. Estili, Y. Sakaida, Two-dimensional molybdenum carbides: Potential thermoelectric materials of the MXene family, Phys. Chem. Chem. Phys. 16 (2014) 7841–7849, doi:10.1039/C4CP00467A.
[25] J.H. Li, Z.X. Sun, W.D. Song, Z.P. Jin, Y.D. Zhan, H. Yin, Z.F. Huang, B.X. Wang, Q.W. Shi, Y.N. Xie, Defect engineering for flexible n-type $Mo_2TiC_2T_x$ o-MXene thermoelectric efficiency enhancement, ACS Appl. Mater. Interfaces 17 (2025) 26984–26993, doi:10.1021/acsami.5c01220.
[26] Z. Jing, H. Wang, X. Feng, B. Xiao, Y. Ding, K. Wu, Y. Cheng, Superior thermoelectric performance of ordered double transition metal MXenes: $Cr_2TiC_2T_2$ (T = –OH or –F), J. Phys. Chem. Lett. 10 (2019) 5721–5728, doi:10.1021/acs.jpclett.9b01827.
[27] R. Kumar, B. Muralidharan, Theoretical insights into the thermoelectric performance of 2D MXene Ti_3C_2, J. Appl. Phys. 137 (2025) 094301, doi:10.1063/5.0252727.
[28] G. Ying, S. Kota, A.D. Dillon, A.T. Fafarman, M.W. Barsoum, Conductive transparent V_2CT_x (MXene) films, FlatChem 8 (2018) 25–30, doi:10.1016/j.flatc.2018.03.001.
[29] J. Tang, R. Zhu, Y.H. Pai, Y. Zhao, C. Xu, Z. Liang, Thermoelectric modulation of neat $Ti_3C_2T_x$ MXenes by finely regulating the stacking of nanosheets, Nano-Micro Lett. 17 (2025) 93, doi:10.1007/s40820-024-01594-z.
[30] R. Li, L. Zhang, L. Shi, P. Wang, MXene Ti_3C_2: An effective 2D light-to-heat conversion material, ACS Nano 11 (2017) 3752–3759, doi:10.1021/acsnano.6b08415.
[31] S. Kumar, U. Schwingenschlögl, Thermoelectric performance of functionalized Sc_2C MXenes, Phys. Rev. B 94 (2016) 035405, doi:10.1103/PhysRevB.94.035405.
[32] A. Es-Smairi, Y. El Krimi, R. Masrour, Sc_2CX_2 (X = O, S, Se) 2D-MXene materials for thermoelectric applications: A DFT study, Mater. Sci. Semicond. Process 188 (2025) 109131, doi:10.1016/j.mssp.2024.109131.
[33] O. Soltani, M.S. Akhoundi Kezrabad, A. Shokri, A. Saffarzadeh, Electronic and quantum transport properties of $Ti_3C_2O_2$ MXene nanoribbons, Diam. Relat. Mater. 161 (2026) 113070, doi:10.1016/j.diamond.2025.113070.
[34] M.S. Akhoundi Khezrabad, O. Soltani, A. Shokri, The effect of edge configurations diversity on the energy gap in MXene zigzag nanoribbons based on $Ti_3C_2O_2$ and $Sc_3C_2F_2$, J. Electron Spectrosc. Relat. Phenom. 279 (2025) 147526, doi:10.1016/j.elspec.2025.147526.
[35] A. Mostafaei, E. Heidari Semiromi, A tight-binding model for the electronic structure of MXene monolayers, Nanoscale 14 (2022) 11760–11769, doi:10.1039/D2NR00745B.
[36] O. Soltani, M.R. Jafari, Comparative study of gate-modulated electronic states in MXenes: Contrasting transport behaviors of Ti_2CO_2, Zr_2CO_2, and Sc_2CF_2, Comput. Mater. Sci. 265 (2026) 114535, doi:10.1016/j.commatsci.2026.114535.
[37] O. Soltani, M.R. Jafari, Strain-tunable electronic transport in MXenes for sensing and stable electronics, Sci. Rep. 16 (2026) 9355, doi:10.1038/s41598-026-40587-3.
[38] Y.T. Du, X. Kan, F. Yang, L. Gan, U. Schwingenschlögl, MXene/graphene heterostructures as high-performance electrodes for Li ion batteries, ACS Appl. Mater. Interfaces 10 (2018) 32867–32873, doi:10.1021/acsami.8b10729.
[39] Y. Liu, J. Yu, D. Guo, Z. Li, Y. Su, $Ti_3C_2T_x$ MXene/graphene nanocomposites: Synthesis and application in electrochemical energy storage, J. Alloys Compd. 815 (2020) 152403, doi:10.1016/j.jallcom.2019.152403.
[40] S. Iravani, A. Zarepour, E.N. Zare, P. Makvandi, A. Khosravi, A. Zarrabi, Synergistic advancements: Exploring MXene/graphene oxide and MXene/reduced graphene oxide composites for next-generation applications, FlatChem 48 (2024) 100759, doi:10.1016/j.flatc.2024.100759.
[41] D.A. Areshkin, C.T. White, Building blocks for integrated graphene circuits, Nano Lett. 7 (2007) 3253–3259, doi:10.1021/nl070708c.
[42] V. Barone, O. Hod, G.E. Scuseria, Electronic structure and stability of semiconducting graphene nanoribbons, Nano Lett. 6 (2006) 2748–2754, doi:10.1021/nl0617033.
[43] Y. Matsuda, W.Q. Deng, W.A. Goddard III, Contact resistance for "end-contacted" metal-graphene and metal-nanotube interfaces from quantum mechanics, J. Phys. Chem. C 114 (2010) 17845–17850, doi:10.1021/jp806437y.
[44] Z.W. Tan, J.S. Wang, C.K. Gan, First-principles study of heat transport properties of graphene nanoribbons, Nano Lett. 11 (2011) 214–219, doi:10.1021/nl103508m.
[45] S. Datta, Electronic transport in mesoscopic systems, Cambridge University Press, Cambridge, 1995.
[46] M. Brandbyge, J.L. Mozos, P. Ordejón, J. Taylor, K. Stokbro, Density-functional method for nonequilibrium electron transport, Phys. Rev. B 65 (2002) 165401, doi:10.1103/PhysRevB.65.165401.

[47] G.J. Snyder, E.S. Toberer, Complex thermoelectric materials, Nat. Mater. 7 (2008) 105–114, doi:10.1038/nmat2090.
[48] C.M. Finch, V.M. Garcia-Suarez, C.J. Lambert, Giant thermopower and figure of merit in single-molecule devices, Phys. Rev. B 79 (2009) 033405, doi:10.1103/PhysRevB.79.033405.
[49] O. Karlström, H. Linke, G. Karlström, A. Wacker, Increasing thermoelectric performance using coherent transport, Phys. Rev. B 84 (2011) 113415, doi:10.1103/PhysRevB.84.113415.
[50] N. Mingo, Calculation of Si nanowire thermal conductivity using complete phonon dispersion relations, Phys. Rev. B 68 (2003) 113308, doi:10.1103/PhysRevB.68.113308.
[51] G. Chen, Nanoscale energy transport and conversion, Oxford University Press, Oxford, 2005.
[52] L.D. Hicks, M.S. Dresselhaus, Effect of quantum-well structures on the thermoelectric figure of merit, Phys. Rev. B 47 (1993) 12727–12731, doi:10.1103/PhysRevB.47.12727.
[53] A. Wang, S. Li, X. Zhang, H. Bao, Roles of electrons on the thermal transport of 2D metallic MXenes, Phys. Rev. Mater. 6 (2022) 014009, doi:10.1103/PhysRevMaterials.6.014009.
[54] O. Soltani, Code for MXene thermoelectric properties, GitHub, 2026. https://github.com/omidsoltani1369/cmse-paper-MXene.